



PAPER • OPEN ACCESS

Universal gate-set for trapped-ion qubits using a narrow linewidth diode laser

To cite this article: Nitzan Akerman *et al* 2015 *New J. Phys.* **17** 113060

View the [article online](#) for updates and enhancements.

Related content

- [Coherent Manipulation](#)
U G Poschinger, G Huber, F Ziesel *et al.*
- [The coherence of qubits based on single ions](#)
F Schmidt-Kaler, S Gulde, M Riebe *et al.*
- [High-fidelity state detection and tomography of a single-ion Zeeman qubit](#)
A Keselman, Y Glickman, N Akerman *et al.*

Recent citations

- [Micromotion-enabled improvement of quantum logic gates with trapped ions](#)
Alejandro Bermudez *et al*
- [Trapped-Ion Quantum Logic with Global Radiation Fields](#)
S. Weidt *et al*
- [Atomic Quadrupole Moment Measurement Using Dynamic Decoupling](#)
R. Shaniv *et al*



OPEN ACCESS

RECEIVED
10 May 2015REVISED
30 September 2015ACCEPTED FOR PUBLICATION
2 October 2015PUBLISHED
27 November 2015

Content from this work
may be used under the
terms of the [Creative
Commons Attribution 3.0
licence](#).

Any further distribution of
this work must maintain
attribution to the
author(s) and the title of
the work, journal citation
and DOI.



PAPER

Universal gate-set for trapped-ion qubits using a narrow linewidth diode laser

Nitzan Akerman, Nir Navon¹, Shlomi Kotler², Yinnon Glickman and Roe Ozari

Department of Physics of Complex Systems, Weizmann Institute of Science, Rehovot 76100, Israel

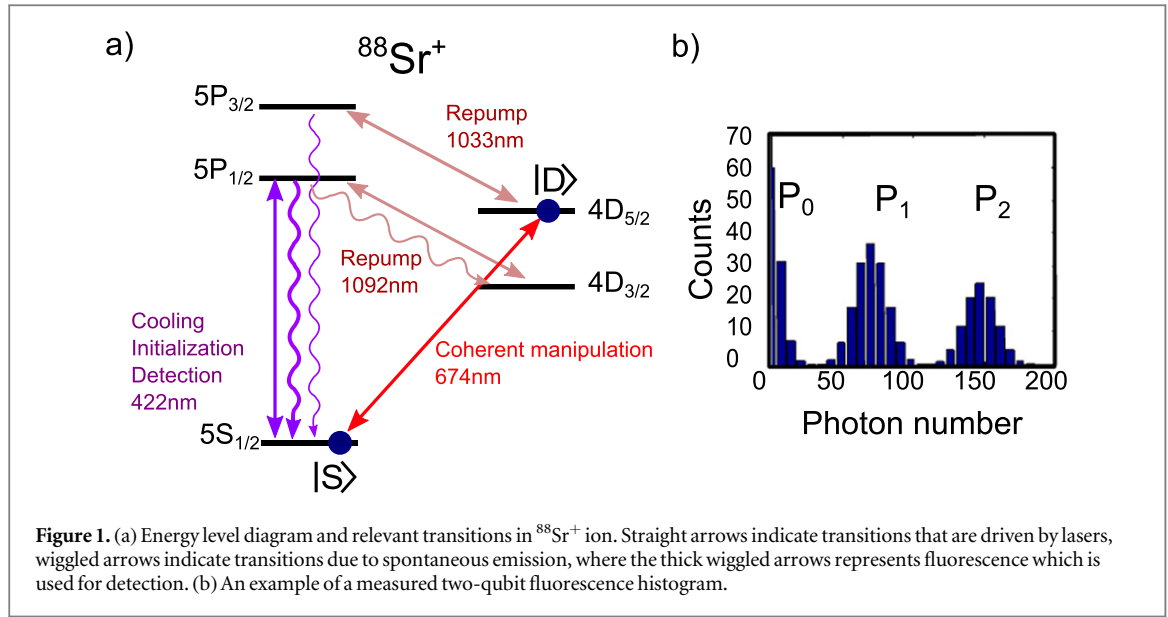
¹ Present address: Cavendish Laboratory, University of Cambridge, J.J. Thomson Ave., Cambridge CB3 0HE, UK.² Present address: Physical Measurement Laboratory, National Institute of Standards and Technology, Boulder, CO 80305, USA.E-mail: nitzan.akerman@weizmann.ac.il**Keywords:** quantum information, trapped ions, universal gate set**Abstract**

We report on the implementation of a high fidelity universal gate-set on optical qubits based on trapped $^{88}\text{Sr}^+$ ions for the purpose of quantum information processing. All coherent operations were performed using a narrow linewidth diode laser. We employed a master-slave configuration for the laser, where an ultra low expansion glass Fabry–Perot cavity is used as a stable reference as well as a spectral filter. We characterized the laser spectrum using the ions with a modified Ramsey sequence which eliminated the affect of the magnetic field noise. We demonstrated high fidelity single qubit gates with individual addressing, based on inhomogeneous micromotion, on a two-ion chain as well as the Mølmer–Sørensen two-qubit entangling gate.

1. Introduction

The coherent manipulation of systems at their quantum level is an essential capability in many fields such as quantum information processing (QIP), quantum simulation and metrology. One aspect that separates a quantum system from its classical counterpart, is an exponential increase of state space as a function of the physical size of the system. The realization of arbitrary quantum operations on large systems is therefore a complicated task. Nevertheless, as in classical computation, any complex quantum operation can be approximately performed, with arbitrary accuracy, by concatenating operations taken from a finite set of simple gates. The finite set of gates from which any unitary operator can be constructed is called a universal gate set [1–3]. In the case of N two-level systems (a register of N -qubits), a universal gates set, for instance, may be comprised of a discrete and finite set of single qubit rotations and a two-qubit controlled-not gate [4]. While it should be possible to apply each of these gates to any qubit, or qubit-pair, in the register, the number of gate types does not depend on the number of qubits involved.

Trapped-ion qubits are one of the most promising platforms for QIP. Ions can be trapped for long times and laser-cooled to their ground motional state. Their internal electronic state as well as their motion can be controlled with high precision using lasers, microwave and radio-frequency fields [5, 6]. Owing to the isolation of trapped ions from their surrounding, quantum states can have an extremely long coherence time [7]. Techniques for single-qubit rotations have been mastered for many years in atomic spectroscopy and have been demonstrated using trapped-ion qubits with extremely low error rates [8, 9]. The individual addressing of qubits within a crystal of closely-spaced ions and the entanglement of two ion qubits are more challenging tasks. Both tasks require control field gradients on the order of the separation between ions, i.e. in the micrometer range. Solutions to this problem involve high static magnetic field gradient [10, 11] or near-field microwave radiation [12]. Both schemes are promising for future scaling up of ion trap technology since here the control fields can be generated by electrodes that are integrated into the trap structure itself. Entanglement gate fidelities with these approaches [6, 13], however, have not yet matched the ones realized with laser driven gates. The more traditional approach for realizing the gates above relies on optical fields. Here, typical control field gradients are determined by the wavelength used and are typically below one micrometer. Entanglement gate fidelities using laser control



fields were recently demonstrated with errors under one percent [14, 15]. Implementing parallel optical gate control in a large scale, multi-zone, ion trap however is a non-trivial task. Ways must be found to compactly route and switch laser beams between different trapping zones. To this end various efforts have been directed towards the development of micro-mechanical mirrors [16, 17] and the integration of fibers into trap structures [17]. Also, unlike microwave and radio-frequency sources, lasers are typically large and power consuming. A future quantum technology will benefit from the development of gates that are generated by small, compact, and low power-consuming laser technology.

In this paper we present a complete set of operations on a two ion qubit register that are based on diode laser control. Diode lasers are compact, low-cost, and low power consuming coherent light sources. The gates performed include single qubit rotations and a two-qubit entangling gate. The relevant internal states and transitions in a $^{88}\text{Sr}^+$ ion are depicted in figure 1. We encoded quantum information in two optically separated manifolds in the $|S\rangle = |S_{1/2, m=+1/2}\rangle$ and $|D\rangle = |D_{5/2, m=+3/2}\rangle$ states. The two manifolds are coupled by a quadrupole transition where the excited $D_{5/2}$ level has a lifetime of 390 ms. Driving coherent operations between the two manifolds was accomplished using a narrow linewidth 674 nm laser in a master-slave configuration. Due to the finite Lamb–Dicke parameter $\eta_{674} \approx 0.04$ the motional degrees of freedoms of the ion can be accessed as well. This is a necessary capability since getting the two qubits to interact can be efficiently done only through their Coulomb interaction. The scheme that was implemented here for entangling two ions, is the Mølmer–Sørensen (MS) gate. Incoherent operations such as cooling, preparation and detection were performed on the $S_{1/2} \rightarrow P_{1/2}$ electric-dipole transition using a 422 nm light in addition to two repumps at 1092 nm and 1033 nm in order to deplete the population in the $D_{5/2}$ and $D_{3/2}$ levels, respectively. State initialization to the $|S\rangle$ state was done by optical pumping with circularly polarized light. Detection was carried out by counting fluorescence photon using a photomultiplier tube for a typical duration of 1 ms. State discrimination relies on the fact that only population in the $S_{1/2}$ contributes to the fluorescence. From the statistics of the counted photons the probabilities of having zero, one and two qubits (for two-qubit register) in the $|S\rangle$ state were inferred. An example of such histogram is shown in figure 1(b). In this work, the typical infidelity due to state preparation and detection were around 5×10^{-3} . More details on our experimental apparatus can be found in [18, 19].

Manipulating optical qubits requires a narrow linewidth laser. As an example, the dephasing time of optical qubits will be limited by the inverse of the laser linewidth as the laser itself constitutes the local oscillator reference. Stabilized diode lasers are a relatively simple and cheap option for the realization of narrow linewidth lasers. Their use has been growing in popularity in the field of precision measurements and in particular, in atomic clocks where sub-Hz linewidth has been obtained [20–22]. Using narrow linewidth lasers for coherent operations on trapped ions poses slightly different requirements than atomic clocks as the former is highly sensitive to the spectral purity of the laser at a larger bandwidth i.e. in some operations, as two qubit gate, the laser is tuned to the motional sidebands which are few MHz away from the carrier transition resonance. Therefore any spectral noise at this range will drive undesired carrier transitions that will reduce the fidelity of the gate. In our case, the main contribution to the noise at this spectral range arises from the servo loop which locks the master laser to a stable high-finesse cavity [23]. When the fast feedback is based on current modulation

of the diode laser the typical unity gain, at which the induced noise is maximal, is at about 1 to 2 MHz. As we will show, a way to overcome this problem is to utilize the light that is transmitted through the cavity. With a linewidth of several kHz, the cavity functions as a narrow optical filter which reduces the high frequency noise significantly.

2. Narrow linewidth diode laser

2.1. The master laser

Light is generated by an external cavity diode laser (ECDL, Toptica DL100) that is locked to a high-finesse Fabry–Perot cavity which is made of ultra-low expansion glass (ULE). The ECDL, with a 10 cm long cavity, produces 10 mW of power at 674 nm and is enclosed in an acoustically-isolated box. The laser frequency is stabilized to a cavity resonance by means of the Pound–Drever–Hall (PDH) locking technique [24]. A single mode polarization maintaining (PM) fiber guides the light from within the box to the optical table where sidebands at 20 MHz are added to the laser spectrum by phase modulation using an electro-optic modulator. Roughly 500 μ W of light is sent by a PM fiber to the ULE cavity which is mounted on a separate breadboard. A polarizing beam splitter (PBS) and a $\lambda/4$ retardation plate direct the reflected light from the cavity toward a 100 MHz bandwidth photo-detector to produce the PDH beat signal. The beat signal is demodulated and fed into a fast analog controller (Toptica PDD and FALC modules) to optimize the transfer function of the servo loop. The output from the controller is fed-back into a field-effect transistor (FET) connected in parallel with the diode laser inducing current changes, which in turn steer the laser frequency. Due to the limited dynamic range of the FET, another feedback loop, implemented on a field programmable gate array, keeps the average voltage of the FET fixed by controlling the voltage on the piezoelectric transducer that controls the ECDL grating angle.

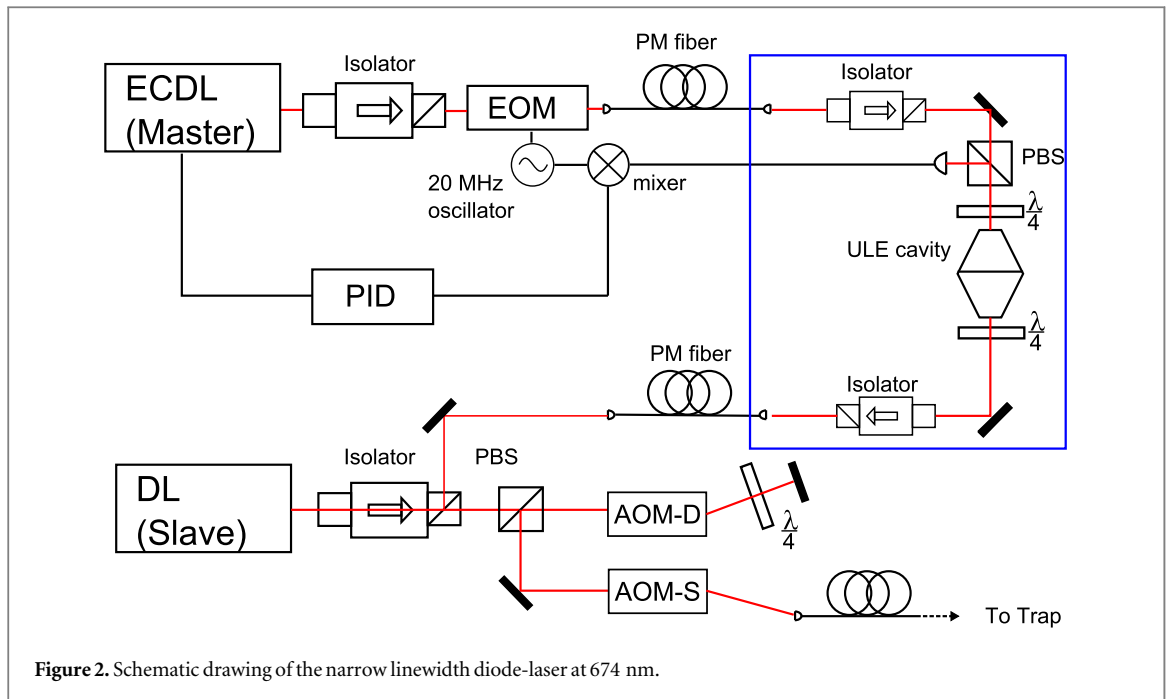
The ULE reference cavity (Advanced Thin Films Inc.) has a finesse of $\mathcal{F}=10^5$ measured using ring-down spectroscopy. The cavity is placed in a vacuum chamber at a pressure of 10^{-7} Torr. Viton rubber pads are used to reduce acoustic vibrations. The free spectral range of the cavity longitudinal modes is 1.93 GHz and the cavity linewidth is $\Gamma_c = 22$ kHz. The cavity is thermally isolated by the vacuum environment and a thermal isolation material which is wrapped around the vacuum chamber. The resulting peak-to-peak amplitude of the cavity frequency drift at 674 nm is about 1 MHz over a time scale of hours and the maximal slope is about 2 kHz per minute. Since the laser has to be tuned to the atomic transition frequency with sub kHz accuracy, we scan the atomic transition every three minutes and by linear interpolation evaluate the cavity resonance frequency and adjust the laser frequency accordingly at the beginning of each experiment.

2.2. Laser frequency and amplitude control

The various operations on the optical qubit set a few requirements on the laser frequency control setup which is based on acousto-optic modulators (AOM):

- (i) Frequency detuning range up to the trap driving frequency of 21.75 MHz.
- (ii) Driving two frequencies simultaneously for the MS-gate.
- (iii) Shifting all the above output frequencies to compensate for slow ULE cavity drifts.
- (iv) Keeping a controlled phase relation between the various frequencies.

To satisfy all demands the use of two AOMs is unavoidable. One is in a double-pass configuration and the other is in a single-pass configuration. While the double-pass allows for a wider range of detuning it can not be used to produce a bichromatic beam. This is because when the beams are retro-reflected in the second pass they will diffract from both frequencies that drive the AOM, leading to a third beam with frequency shift of $f_1 + f_2$ which is unwanted. Therefore, the bichromatic beams are generated with the single-pass AOM. We use a separate frequency source for almost each frequency in the experiment in order to control the phase relation between the various frequencies. The alternative of using a single frequency source and varying its frequency will introduce phase noise due to time jitter in the frequency updating time. The schematic diagram of our frequency sources is presented in figure 3. The double pass AOM has three frequency sources which are all based on direct digital synthesizers (DDS, Novatech 409). An rf switch is used to choose between the carrier frequency and the micro-motion (MM) sideband frequency (used for single qubit addressing which is explained in the next section) separated by 21.75/2 MHz. The two frequencies are shifted by the base frequency electronically with a mixer where the fundamental frequencies are filtered by a bandpass filter. We use the base frequency to correct for the ULE drifts without the need to update both the carrier and MM-sideband DDSs which would introduce relative phase noise between them. The single pass AOM has four frequency sources. The red sideband (RSB) and blue sideband (BSB) generate the bichromatic beam for the two-qubit entangling gate. $F1$ is used to drive



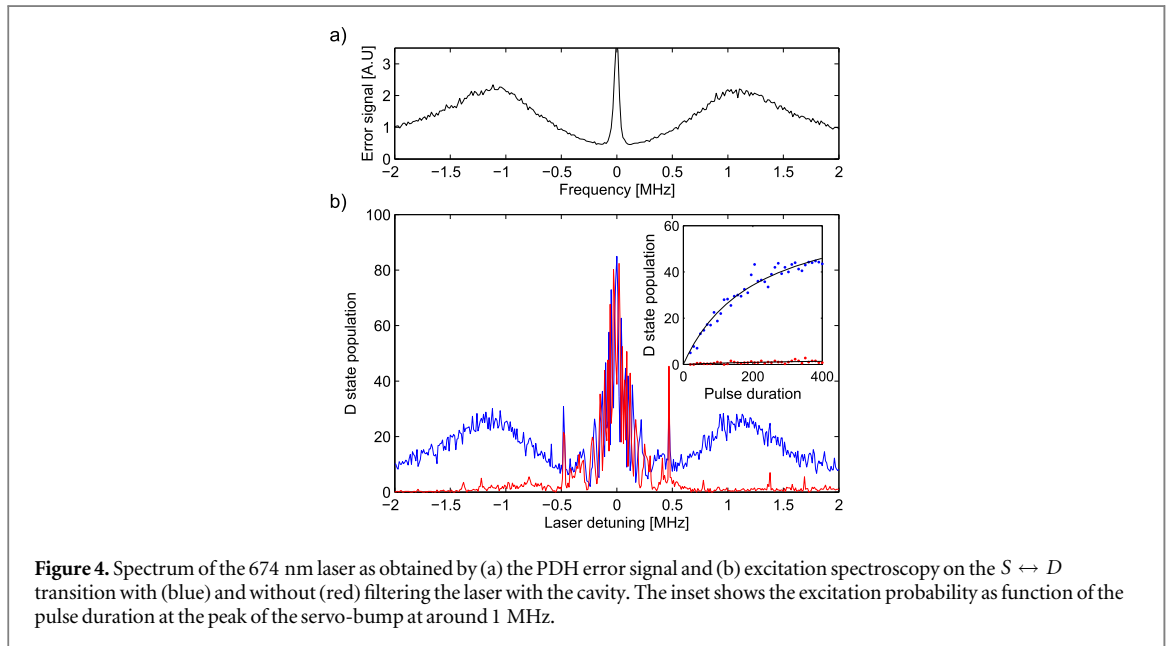
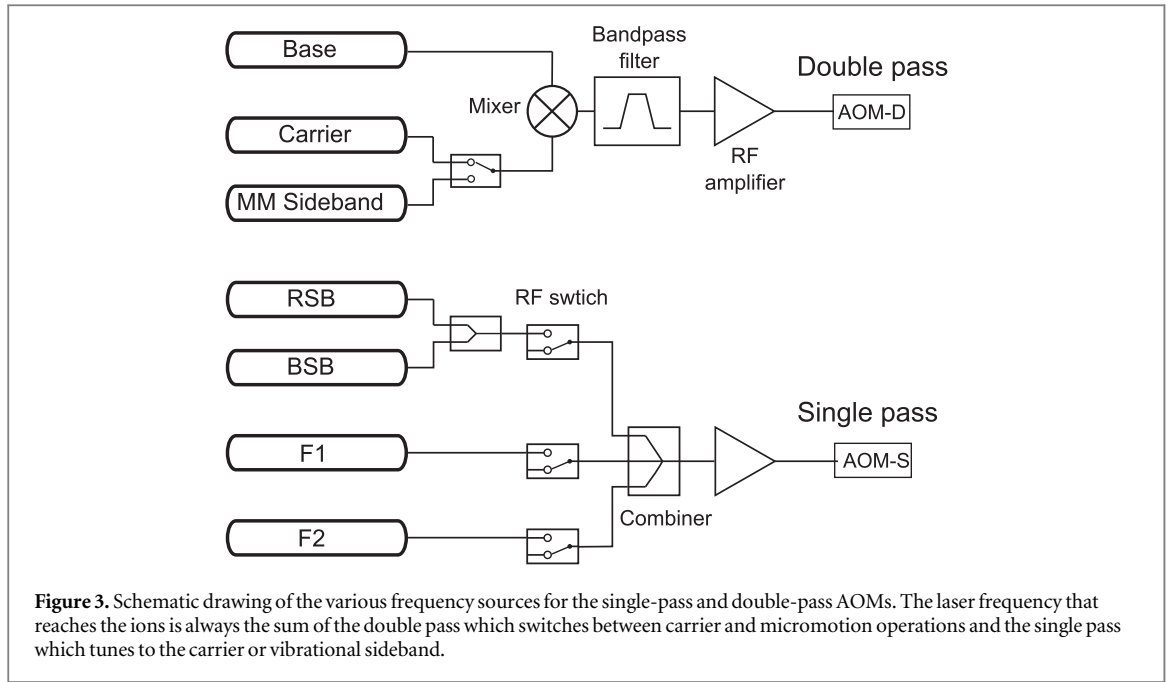
carrier transition with a well defined phase with respect to the RSB and BSB. The last frequency source $F2$ is a DDS that updates its output frequency in real-time to drive operations with no phase relation requirement such as electron shelving for state detection and ground-state cooling.

2.3. Laser high-frequency noise—servo bumps

The bandwidth of the laser-cavity locking servo was found to be limited by the response of the laser diode to current modulation. Increasing the servo gain to reduce the laser linewidth is impeded by the growth of oscillations around the frequency of inverse feedback phase. Even when the gain at this frequency is kept below unity to maintain stability, noise around this frequency is amplified. These amplified noise bands around the unity gain frequency are known also as 'servo-bumps'. In our system these servo-bumps are located at about 1 to 2 MHz and have FWHM of about 1 MHz. We observed servo-bumps in the spectral content of the laser experimentally in two different ways. The first is a direct measurement of the PDH error signal spectrum with an rf spectrum analyzer. This measurement result is plotted in figure 4(a). Secondly, we measured the ion response to an excitation of the quadrupole transition. Here, the laser frequency was scanned across the transition and the population in the $D_{5/2}$ state was measured. The duration of the excitation pulse was set to 100 μ s, and the laser propagation direction was perpendicular to the axial direction of the trap to avoid coupling to the axial motion of the ion in the trap. The result of this measurement is presented by the blue solid line in figure 4(b). The fast oscillations around the central resonant peak are due to the 100 kHz Rabi frequency which results in many oscillations during the 100 μ s pulse. The additional narrow peaks at around 0.5 MHz are due to second harmonic of a radial sideband of a transition between different Zeeman states. Both the Rabi spectroscopy and the spectrum analyzer are showing a similar feature of a 1 MHz wide response around ± 1.1 MHz from resonance. This wide response is attributed to incoherent excitation of the carrier transition due to the servo-bumps in laser spectrum. This spectral feature has undesired consequences when driving vibrational sidebands transitions that are typically detuned by a 1 to 2 MHz from the carrier. In this case the servo-bump will drive incoherently the carrier transition and lead to decoherence. For example, we have observed that the fidelity of the MS entangling gate is severely compromised by this effect.

One way to eliminate the harmful effect of the servo-bump is to improve the performance of the servo loop by increasing its bandwidth. In this case the unity-gain frequency, and hence the servo-bumps, will be shifted towards a higher frequency and away from the motional sidebands. This can be done, for example, by introducing an intra-cavity EOM into the ECDL [25]. Here, we have taken another approach in which we optically filter those servo-sidebands from the laser spectrum [23]. Fortunately, the cavity itself acts as the narrow bandpass optical filter with a 22 kHz width Lorentzian transfer-function. Hence, the light that is transmitted through the cavity possesses high spectral purity with, in principle, three orders of magnitude reduction in the noise spectral power density around the 1 MHz servo-bumps.

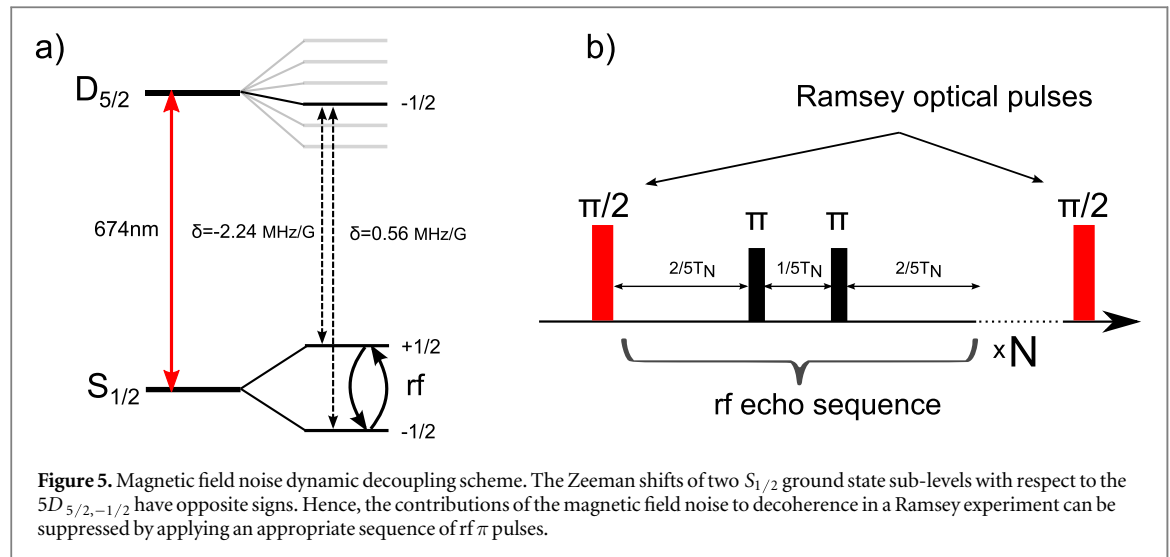
The price for relying on the transmitted light is the attenuation in the available light intensity. In our setup, the cavity transmission is only about 5%. While a decrease by a factor of two can be accounted for spatial mode-



mismatch, most of the loss is due to intra-cavity losses. In addition, the intensity of the light that is sent to the cavity is limited to the mW range in order to prevent substantial thermal effects on the cavity mirrors (ULE substrate) that would in turn lead to thermal shifts of the cavity resonance frequency. Overall the transmitted light intensity is limited to few 10's of μW , which is well below the required intensity for ion-qubit operations, and hence needs to be amplified. To this end, we incorporate another slave diode-laser which is injection-locked to the filtered master-laser light. A slave diode rather than a tapered amplifier is chosen due to the much smaller intensity that is needed to injection lock a diode as compared with the intensity that is required to saturate a tapered amplifier.

The complete master-slave setup is shown in figure 2. The transmitted light polarization is restored to linear by another $\lambda/4$ plate and coupled to a PM-fiber. Two optical isolators are placed at the input and output of the cavity to prevent optical interference. Between 5 to 10 μW of filtered light is injected to the slave diode laser using mode-matching optics. This intensity is sufficient for a stable operation of the slave laser with an injected current window of 0.1 mA.

Intensity fluctuations of the 674 nm light lead to fluctuations in the Rabi frequency, and therefore affect any coherent operation. The origin of intensity noise is mainly due to fiber phase noise that is translated to intensity



noise when passing through a PBS on the way to the ion. To prevent this, the intensity of the laser is monitored close to the input port of the vacuum chamber and stabilized by adjusting the rf power that drives the AOM.

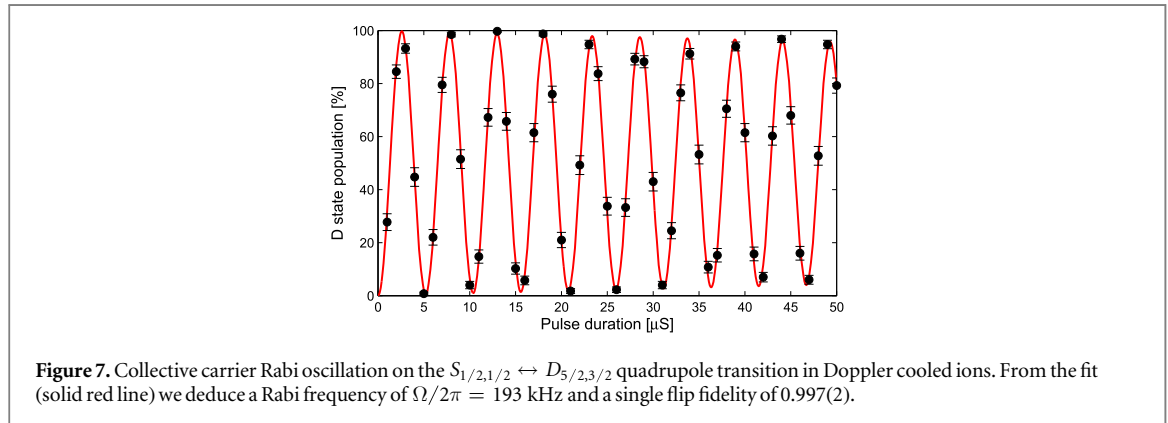
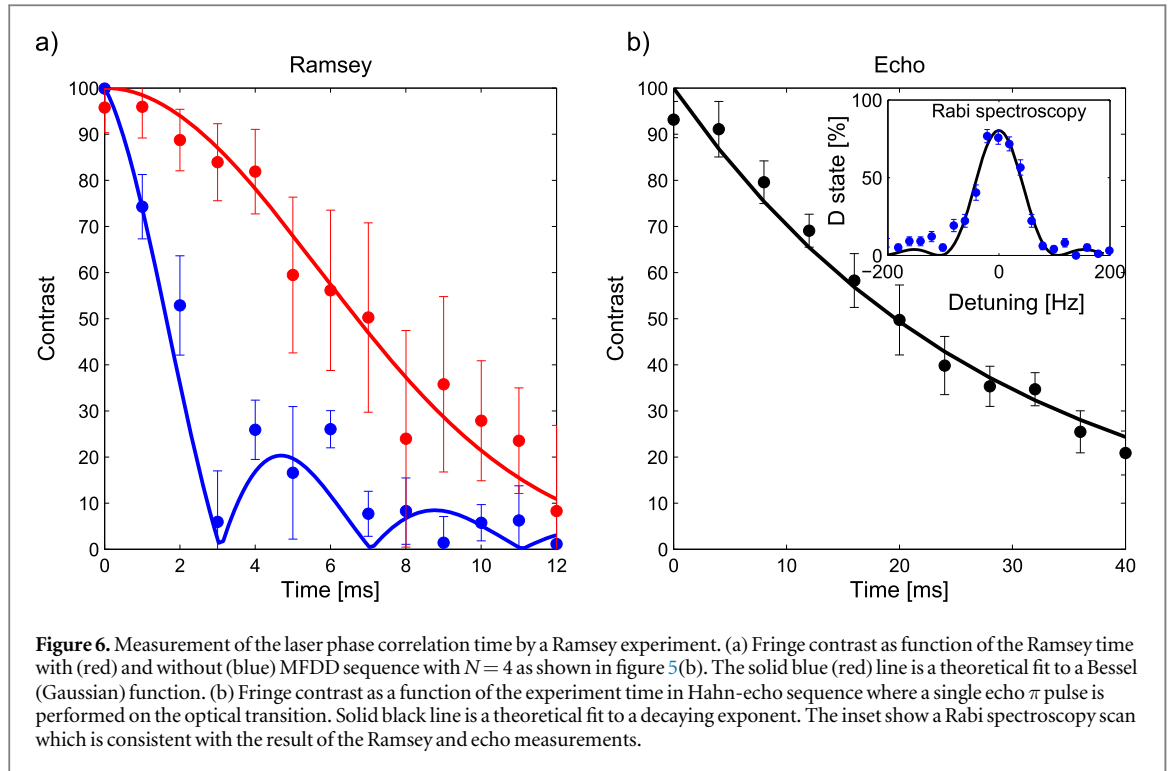
Figure 4(b) compares between the excitation spectrum of the ion when excited with the slave laser when it is injection locked to the unfiltered master laser (blue curve) and to the cavity filtered light (red curve). The significant improvement in the spectral purity is clearly observed. The inset shows a measurement of the excitation probability as function of the pulse duration at the maximum of the servo-bump in the two cases. In the unfiltered light case already at a pulse duration of 400 μ s the population is saturated close to 50% while in the filtered light case as little as 1% to 2% are observed. The ratio between the slopes of the two curves in the linear regime is about 50 which should be regarded only as a lower bound due to the small signal in the filtered case which could be a result of power broadening together with other decoherence mechanisms such as magnetic field fluctuations or leakage of the 1033 nm repump light.

2.4. Characterization of the laser linewidth

In QIP the qubit coherence time is determined by the stability of the relative phase between the qubit and the local oscillator. In the case of an optical qubit, the local oscillator that keeps track of the qubit phase, is a narrow linewidth laser. The physical mechanisms that cause phase fluctuations to the qubit and the laser are different and uncorrelated. Therefore, reaching a long coherence time requires that the phases of both the qubit and the oscillator are independently stable. While commercially available oscillators at radio and microwave frequencies can easily reach coherence times of many seconds (requiring fractional frequency uncertainty of 10^{-6} – 10^{-9}), obtaining a laser with a coherence time of one second, i.e. 1 Hz linewidth, is a much more challenging task and requires fractional frequency uncertainty of 10^{-14} – 10^{-15} . On the qubit side, the dominant source of dephasing are fluctuations of the ambient magnetic field.

One method of characterizing the spectral properties of a laser is a delayed self-heterodyne interferometer [26]. Here the laser light interferes with a delayed fraction of itself by using a long optical fiber to create a substantial time delay τ . However, as the spectral resolution of this method is given by $1/\tau$, to measure the sub-kHz frequency fluctuations requires hundreds of kilometers of fiber length which render this method impractical. The alternative is to compare against another stable reference. Examples for such a reference include another independent laser, an ultra stable Fabry–Perot cavity or a narrow atomic transition.

Since the purpose of our laser is to drive the $S_{1/2} \rightarrow D_{5/2}$ transition in $^{88}\text{Sr}^+$ and with no other tool at hand, we inferred our laser linewidth by performing a Ramsey spectroscopy measurements on the ion. One complication that arises in our case is that the relevant quadrupole transition is first order Zeeman sensitive so a conventional Ramsey experiment can not discriminate between the magnetic field noise and the laser frequency noise. Previously, custom-designed entangled state were used to differentiate laser phase noise from magnetic field noise [27] Here we demonstrate a custom-designed dynamic decoupling sequence to this end. The advantage of using dynamic decoupling for this purpose is the simplicity of its implementation. Our magnetic field dynamic decoupling (MFDD) eliminates only phase fluctuations due to slow magnetic field noise, thus rendering the optical transition to an effective clock transition. After initializing to the superposition state $\psi = 1/\sqrt{2} (|S_{1/2,-1/2}\rangle + |D_{5/2,-1/2}\rangle)$ the scheme follows conventional dynamic decoupling methods [28] in the form of echo pulses with two main differences. The first is that the pulses are performed in the $S_{1/2}$ spin manifold and not on the optical transition as this will reverse the effect of the laser frequency noise as well as the



magnetic field noise. The basic idea is illustrated in figure 5 and relies on the opposite sign of the Zeeman shift of the $S_{1/2,-1/2} \leftrightarrow D_{5/2,-1/2}$ transition as compared with the $S_{1/2,1/2} \leftrightarrow D_{5/2,-1/2}$ transition. As long as the magnetic field does not vary between echo pulses, the phase that is accumulated when the ground state population is in the $S_{1/2,-1/2}$ due to an arbitrary Zeeman detuning, can be reversed by transferring the population to the $S_{1/2,1/2}$ state where the phase is accumulated with the opposite sign. The second difference from a regular echo sequence is that the time which is spent in each state is not equal. This is because the magnitude of the Zeeman shift in the two states is different with a ratio of 1:4. The experimental sequence is illustrated in figure 5(b). For a Ramsey experiment of a total time T and N rf echo sequences, each echo sequence is of duration $T_N = T/N$ and is composed of two rf π pulses separated by a time $T_N/5$ at the middle of the sequence. Notice that in terms of the optical transition this scheme is identical to a conventional Ramsey sequence having only two $\pi/2$ pulse with a wait time in between where it is only the ground state part that is manipulated with rf pulses. We have shown, in previous work [29], that the coherence of ground-state superpositions can be maintained for as long as a second using several hundred echo pulses. In general any dynamic decoupling scheme can be adapted for the manipulation of the ground state part. The experimental results are presented in figure 6(a). We plot the Ramsey fringe contrast as a function of the total experiment time for a plain Ramsey sequence (blue dots) and MFDD sequence with $N = 4$ (red dots). The contrast is obtained by scanning the phase of the second $\pi/2$ optical pulse and fitting the data to a sine function with the amplitude and phase as fit parameters. Solid lines are theoretical fits to a Bessel function in the plain Ramsey case and a Gaussian

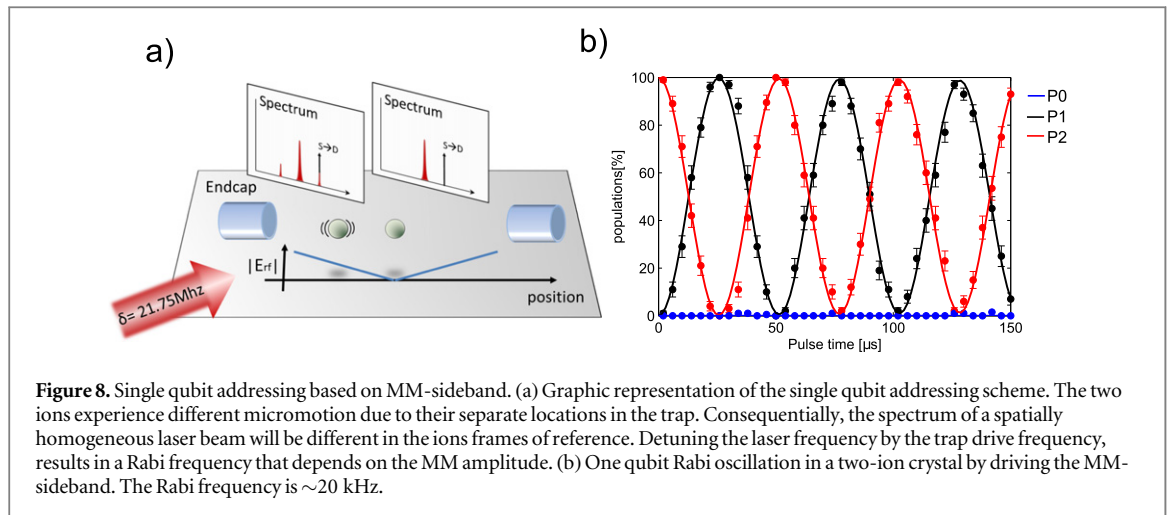


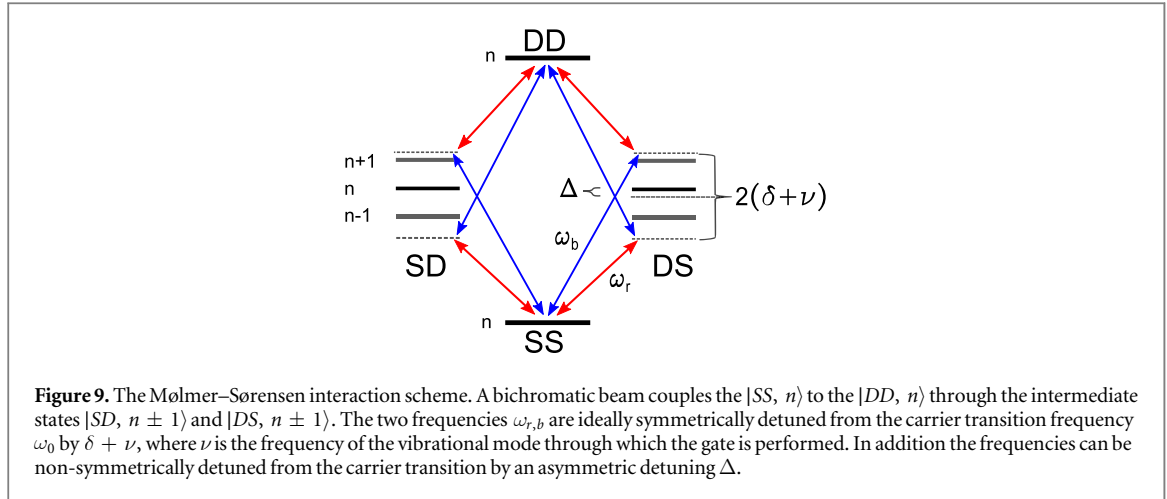
Figure 8. Single qubit addressing based on MM-sideband. (a) Graphic representation of the single qubit addressing scheme. The two ions experience different micromotion due to their separate locations in the trap. Consequently, the spectrum of a spatially homogeneous laser beam will be different in the ions frames of reference. Detuning the laser frequency by the trap drive frequency, results in a Rabi frequency that depends on the MM amplitude. (b) One qubit Rabi oscillation in a two-ion crystal by driving the MM-sideband. The Rabi frequency is ~ 20 kHz.

in the MFDD case. In the regular Ramsey experiment the contrast dropped to 50% after 1.7 ms. Here, the 50 Hz monotone magnetic field noise component dominated and the contrast followed a Bessel shape [30]. Applying the MFDD sequence resulted in a coherence time of 6.7 ms (more than a four-fold improvement) and in addition the contrast follows a Gaussian function shape rather than a Bessel, which implies that there is no single frequency component that dominated the noise spectrum. Applying MFDD sequences with $N > 4$ did not extend the coherence time. Hence, we infer that at this point the laser frequency noise, rather than the magnetic field noise, is the limiting factor. Assuming a Gaussian line-shape, we infer a laser linewidth of 65(5) Hz at integration time of 10 s. More information on the laser spectral content can be obtained by a standard single echo sequence on the optical transition. Here, we did not apply the MFDD sequence but rather incorporated an active stabilization system that reduced the ambient magnetic field noise to a negligible level. As shown in figure 6(b), the contrast extended to 20 ms following exponential decay. Since the echo pulse acts as a high-pass filter we infer that the coherence time measured without the echo is limited by low frequency noise which we assume to have a $1/f$ characteristic. If we consider the echo measurement to represent the laser fast-linewidth (white noise contribution) then from the exponential fit we obtained 11(1) Hz linewidth [31]. Finally, The inset in figure 6(b) shows a Rabi spectroscopy scan using a weak and long excitation pulse with a duration of 11 ms. The spectral feature has a width of 106 ± 20 (Hz) which is consistent with a transform limited result and roughly consistent with the laser linewidth measured using MFDD. In this case the low frequency noise impeded our ability to increase the pulse time and obtain much a narrower feature.

3. Single-qubit gate

For the characterization of single qubit operations in the context of QIP we need to distinguish between operations which are collective and act on all the qubits in the register, and operations that are applied to individual qubits. The former is similar to the case of a single-qubit register in which high fidelity rotation gates that go beyond current estimates for fault tolerance threshold have been demonstrated [8, 9]. In our case, we perform single qubit rotations by driving the optical electric quadrupole transition. Figure 7 shows 20 consecutive collective carrier Rabi flops on a two-qubit register with Rabi frequency of $\Omega_c/2\pi \approx 200$ kHz. The small reduction in the contrast can be attributed to the laser frequency and amplitude noise as well as the motional spectator modes as the ions are only Doppler cooled with axial (radials) secular frequency of 1.95(3.8) MHz. From the fitted decaying envelope we can deduce a single flip (π rotation) fidelity larger than 0.997(2) but a more reliable result would be inferred by performing randomized benchmarking [32] which is beyond the scope of this work.

In the case of more than one qubit, where single qubits need to be addressed individually, the experimental challenges are different. Here only a handful of experiments have demonstrated single qubit addressing and gates with high fidelities [4, 10, 11, 33]. The major challenge here is to apply a high fidelity operation on one qubit while preventing unwanted state changes to the neighboring qubits. The two most popular methods rely on tightly focused laser beams that locally induce a light shift on a single ion qubit and strong magnetic gradients, both lift the degeneracy between the different qubits in the register and allow to individually address the desired qubit in the spectral domain. Our approach uses the readily available spatial variation of the rf electric field amplitude of the ion trap along the axial direction [34]. The basic principle, which is illustrated in figure 8(a), is to utilize the excess micromotion to drive the optical qubit transition. For the case of only two qubits, which is



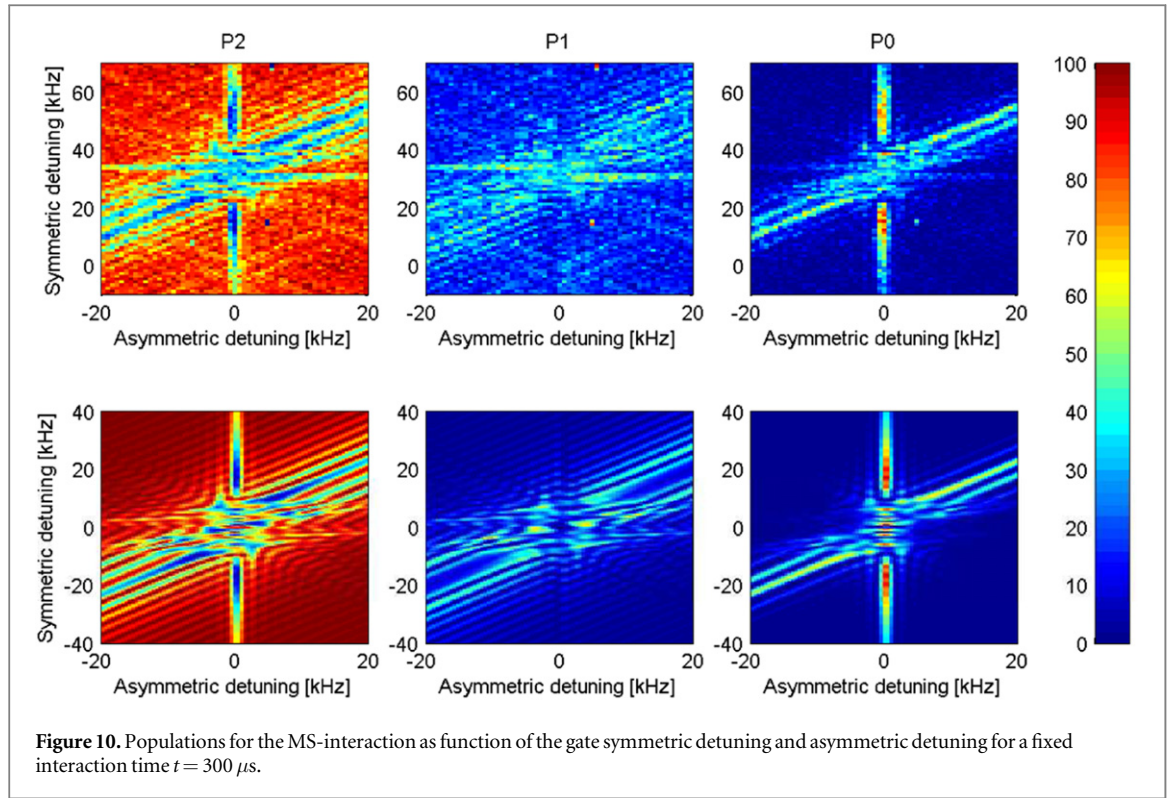
discussed here, we position the two-ion crystal such that one is exactly at the rf null (null-qubit) whereas the other qubit (MM-qubit), which is not at the null, undergoes micromotion at the trap drive frequency of 21.75 MHz. The excess micromotion that we use is along the axial direction of the trap and is due to the boundary conditions that are imposed by the endcap electrodes. In the ion frame of reference, the periodic Doppler shift due to excess micromotion adds sidebands to the laser spectrum. By detuning the laser frequency from the carrier transition by the trap rf frequency, the MM-sidebands can be used to resonantly drive coherent operations on MM-qubit while the Rabi frequency for null-qubit is largely reduced and ideally nulls altogether. The Rabi frequency for driving the MM-sidebands depends on the micromotion amplitude, $\Omega_{MM} = \Omega_c \cdot J_1(\mathbf{x}_{MM} \cdot \mathbf{k})$, where Ω_c is the carrier Rabi frequency in the absence of excess micromotion, J_1 is the first order Bessel function, \mathbf{k} is the laser wavevector and \mathbf{x}_{MM} is the micromotion amplitude vector. When \mathbf{x}_{MM} is much smaller than the laser wavelength the Rabi frequency can be approximated by $\Omega_{MM} = \Omega_c/2 \cdot \mathbf{x}_{MM} \cdot \mathbf{k}$. Moreover, the reduction in carrier Rabi frequency due to the micromotion is second order in the amplitude and can be neglected.

Figure 8(b) shows single qubit Rabi flops by driving the MM-sidebands. The various curves represent the different measured register states $P0$ (blue), $P1$ (black) and $P2$ (red) which correspond to the probabilities of finding zero, one and two qubits in the $|S\rangle$ state. As is expected from only one qubit flopping, $P1$ and $P2$ oscillate with an opposite phase with almost 100% amplitude while $P0$ stays below 1% throughout the measurement. This means that the null-qubit remained in the $|S\rangle$ while the MM-qubit oscillated periodically between the $|S\rangle$ and $|D\rangle$ states with a Rabi frequency of roughly 20 kHz. Here, the axial frequency was lowered to 1 MHz which increased the separation between the ions and therefore the micromotion amplitude and Rabi frequency of the MM-sidebands. In this measurement the single qubit flip (π rotation) fidelity was as high as the collective qubits flips that are presented in figure 7. However, the MM-sidebands gate is not as robust and stable as collective carrier rotations. This is due to the extreme sensitivity of the excess MM to the electrostatic environment where very small changes in the ambient electric fields change the MM-sidebands Rabi frequency and introduce rotation errors. To mitigate the drift in the MM-sidebands Rabi frequency, composite pulses can be applied. As an example, the sequence $X_{\pi/2} Y_{\pi} X_{\pi/2}$ where X, Y are the direction of rotation, implements a π rotation that is first-order insensitive to small variation in the Rabi frequency.

The two operations discussed above: two-qubit collective rotations and individual addressing of only one qubit are sufficient in the case of a two-qubit register to perform any single qubit gate. As an example in [35] we have used this scheme to perform complete quantum process tomography for the MS two qubit gate. In principle the use of the spatially varying electric field and micromotion induced sidebands can be generalized to more than two ions by introducing the concept of dressed-state picture [34].

4. MS two-qubit interaction

Experimentally implementing a universal two-qubit gate is typically more challenging than implementing single-qubit rotations. This is because two-qubit gates require the synthesis of bipartite interactions between qubits. Since trapped ions are separated by a few microns, the interaction between their qubit states is synthesized by coupling their internal states to their quantized collective modes of motion. Here we present our implementation of the MS entangling gate [36] which, together with a universal single qubit rotations, forms a universal gate-set for quantum computation. The MS scheme, besides being successful in reaching fidelities as



high as 99.3% [14], holds some desirable properties such as resilience to finite temperature, straightforward generalization to multi ion-qubit gates and relative simplicity of implementation. The MS interaction scheme is presented in figure 9. It consists of a bichromatic field that drives collective internal state atomic transitions through the RSB and BSBSs of a single vibrational mode. While in general the MS interaction entangles the internal state of the ions with their motion, at certain periodic times the internal states and motion return to be disentangled. At those times the ions internal states undergo collective rotations and the motion returns to its initial state. The interaction Hamiltonian in the rotating wave approximation takes the following form [37]

$$H_{\text{int}} = \frac{\hbar\Omega}{2} \left(i\eta e^{-i\Delta t} (a^\dagger e^{-i\delta t} + a e^{i\delta t}) (\sigma_-^{(1)} + \sigma_-^{(2)}) + \text{h.c.} \right), \quad (1)$$

where Ω is the carrier Rabi frequency and we assume an equal intensity in each of the two beams, η is the Lamb–Dicke parameter, $\delta = (\omega_b - \omega_r)/2 - \nu$ is the bichromatic field symmetric detuning from the motional sidebands, $\Delta = (\omega_b + \omega_r)/2 - \omega_A$ is the bichromatic field asymmetric detuning from the two-photon transition frequency, a and a^\dagger are the creation and annihilation operators of the vibrational normal mode with a frequency ν and $\sigma_{-,+}$ are the ladder operators for the atomic transition.

In the absence of asymmetric detuning, $\Delta = 0$, an analytic expression for the time evolution of atomic populations can be obtained [38]. When starting from the vibrational ground state ($n = 0$) the population dynamics takes the following form

$$P0 = \frac{1}{8} \left(3 + e^{2|\alpha|} - 4e^{|\alpha|/2} \right) + \sin^2(\theta) e^{-|\alpha|^2}, \quad (2)$$

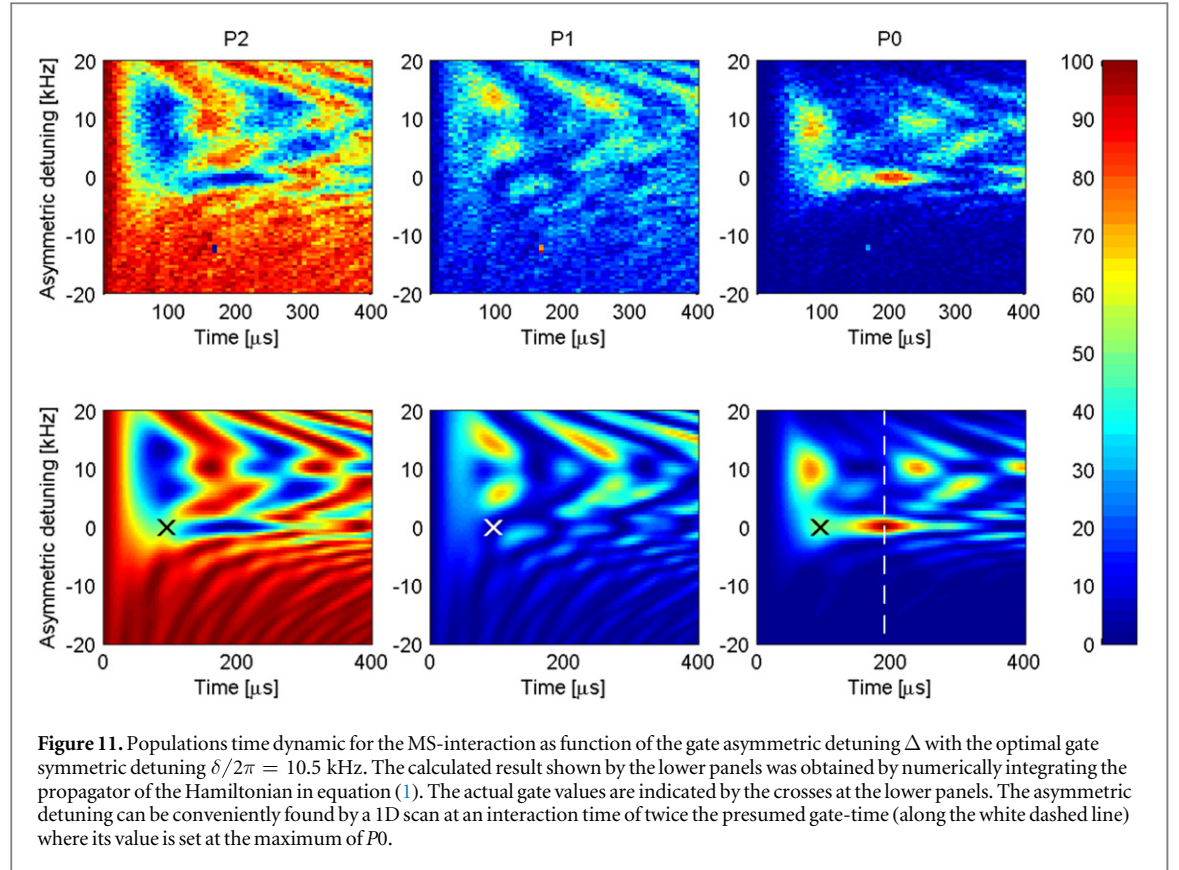
$$P1 = \frac{1}{4} \left(1 - e^{-2|\alpha|^2} \right), \quad (3)$$

$$P2 = \frac{1}{8} \left(3 + e^{2|\alpha|} - 4e^{|\alpha|/2} \right) + \cos^2(\theta) e^{-|\alpha|^2}, \quad (4)$$

where

$$\theta(t) = \frac{\eta^2 \Omega^2 t}{2\delta} (1 - \text{sinc}(\delta t)) \quad \text{and} \quad \alpha(t) = \frac{\eta\Omega}{\delta} (e^{i\delta t} - 1).$$

Starting from the state $|SS\rangle$, a maximally entangled state $|\Phi\rangle = (|SS\rangle + i|DD\rangle)/\sqrt{2}$ is obtained with a detuning of $\delta = 2\eta\Omega$ and after an interaction time of $T_{\text{gate}} = 2\pi/\delta$. In cases where the asymmetric detuning non-zero, the dynamics can be obtained by numerical integration.



4.1. Extensive 2D scans of the MS-interaction parameters

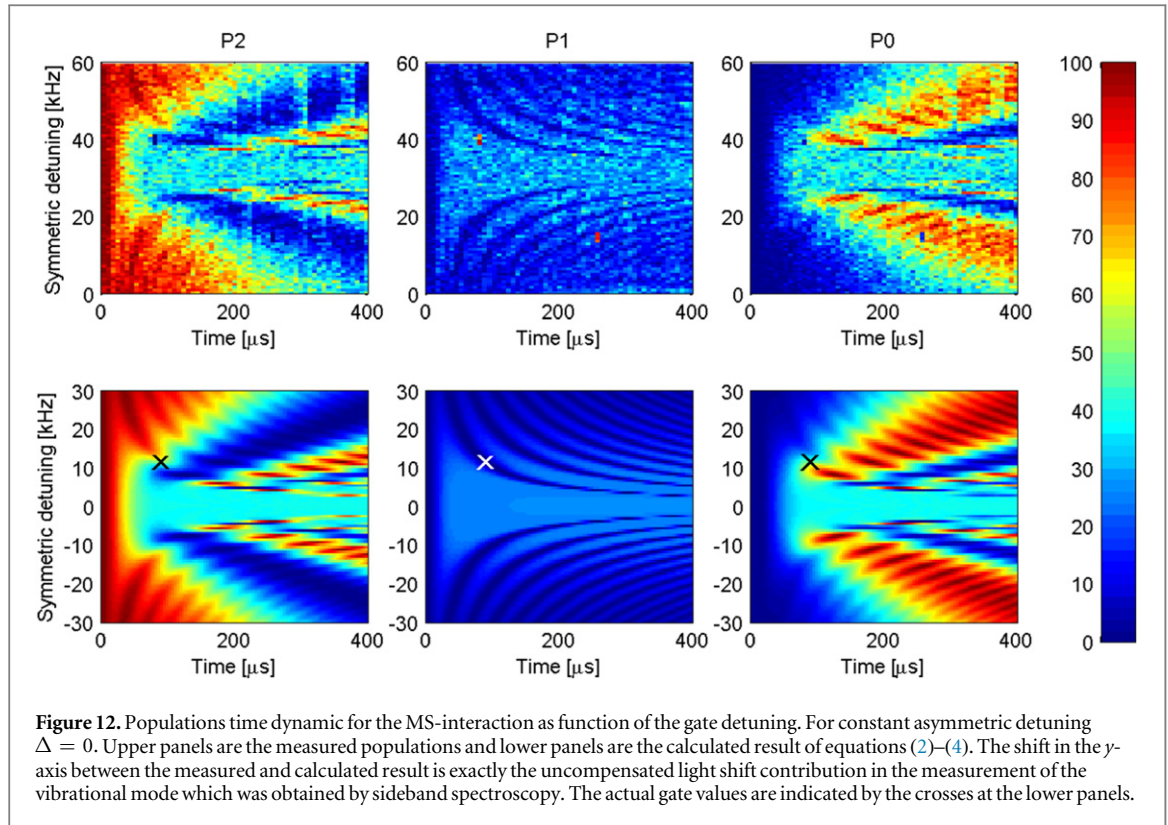
Our experimental implementation of the MS-interaction is similar to that outlined in [38]. A bichromatic beam was produced by single-passing an AOM (AOM-S) which was driven by two rf frequencies (RSB and BSB DDS sources). The beam then propagated to the ions through a PM single mode fiber after which it was focused to a waist of about $20 \mu\text{m}$. At the trap center each spectral component had up to 1 mW of power at 674 nm. At each experiment the two ions were initialized to the $|SS\rangle$ state and their stretched mode which was used for the MS-interaction, was cooled to the ground state ($\bar{n} \approx 0.05$).

As a first step, we examined the ions state population for a wide interval of the interaction parameters: symmetric detuning δ , asymmetric detuning Δ and interaction duration t . Here the center of mass vibrational mode with frequency of $\nu = 0.98$ MHz was used. These scans provide a visual insight to the population dynamics and its dependence of the various parameters of the interaction. In addition, some experimental uncertainties in the gate parameters can substantially effect the gate fidelity. As an example, uncertainties in the intensities of each component in the bichromatic beam, the vibrational mode frequency and light shift from other levels affect the required gate-time and detuning. As shown in [38], the experimental calibration of all these parameters using the gate itself is possible. A different approach, which is more straightforward, however time consuming, is to scan the relevant parameters: symmetric detuning δ , asymmetric detuning Δ and time T_{gate} and measure the two-ion response. Once the experimental maps are obtained the real parameters can be by extracted by comparing the measured maps to the calculated ones. Figures 10–12 present the states population maps, both measured and calculated, for three 2D scans: asymmetric versus symmetric detuning, asymmetric detuning versus time and symmetric detuning versus time.

The practical value of such maps is best demonstrated in the time and symmetric detuning scan which is shown in figure 12. The calculated populations as function of the gate-time and symmetric detuning fully describe the measurement result up to a shift in the detuning of 35 kHz. This large shift is attributed to a bias in our vibrational frequency measurement scheme. Our sideband frequency was measured via sideband spectroscopy using intense beams which generated light shift on the carrier transition frequency which was different in the MS gate beam configuration. Therefore, the measured sideband frequency included a significant light shift of 35 kHz.

4.2. Two-qubit entangling gate

The process of finding the optimal values for the gate parameters begins by inspecting the 2D maps in figure 10 which is comprised of two prominent features. One is the central vertical line which arises from $|SS\rangle \rightarrow |DD\rangle$ two-photon coupling, whereas the diagonal line is a result of a BSB excitation. The opposite diagonal line which



correspond to a RSB transition is absent here since the initial state is the vibrational ground state. From the crossing of the two lines we obtain a rough estimate for both the symmetric and asymmetric detunings. Note that the interaction time in this scan is much longer than the presumed gate-time. In the next step we determine the asymmetric detuning with higher precision. To this end, we scan the asymmetric detuning at a fixed interaction time which is equal to twice the presumed gate-time. This corresponds to the dashed vertical line in the 2D map of P_0 that is presented in figure 11. The asymmetric detuning value is then set by maximizing P_0 . The result hardly depends on the interaction time for relatively large interval as can be seen in the figure. The gate-time and symmetric detuning can be found by performing 2D scan similar to that of figure 12 but with higher resolution and only in the region of the presumed values. The two parameters are fixed at the point where P_1 is minimal (ideally zero) and $P_0 = P_2 \approx 50\%$. The correct values of these two parameters can be obtained more efficiently by an iterative process that consists of two 1D scans. The procedure is illustrated in figure 13. First, we scan the gate symmetric detuning at the presumed gate-time and set it to the value where the populations $P_0 = P_2$ which is represented by the blue curve in the figure. Next, the gate-time is scanned with the obtained gate detuning. Here the gate-time is fixed at the point where P_1 is minimal (represented by the red curve). After iteratively repeating the two scans (black arrows) the process converges and the correct values (black rectangle) are obtained as long as the starting value of the gate-time does not deviate from its actual value by more than about 25% (the plotted region). Having a residual asymmetric detuning of less than 1 kHz modified the two curves but still allows the process to converge although to slightly different values.

Figure 14(a) presents the populations as a function of the interaction time. Here, we used the stretch vibrational mode. At a gate-time of $T_{\text{gate}} = 140 \mu\text{s}$ the ions superposition consists of only the $|SS\rangle$ and $|DD\rangle$ states. To verify that the resulting state is indeed a Bell state, the off-diagonal elements of the density matrix must be measured as well. This was done by applying another $\pi/2$ pulse with a phase ϕ and measuring the state parity $P = P_0 + P_2 - P_1$. The amplitude of parity oscillations, A_p , as function of ϕ is equal to $2 |\rho_{SS,DD}|$. The gate fidelity for producing the Bell state $|\Phi\rangle$ is given by $F_\Phi = (P_0 + P_2)/2 + A_p$. Using the maximum likelihood method to fit the data in figure 14(b), we conclude gate fidelity³ of $F = 0.985(10)$. While part ($\approx 5 \times 10^{-3}$) of the gate error can be attributed to imperfection in the preparation and detection operations, the rest is assumed to arise from error in the gate itself. Although the exact source of error has not been fully identified, the nature of the error has been studied in [35] where we have performed process tomography on five consecutive gates. The

³ The likelihood of the measured data was calculated given a series of binomial distributions with mean values that follow a sinusoidal pattern with a given amplitude and phase. The amplitude and phase that yield the highest likelihood were used as an estimate for the gate fidelity.

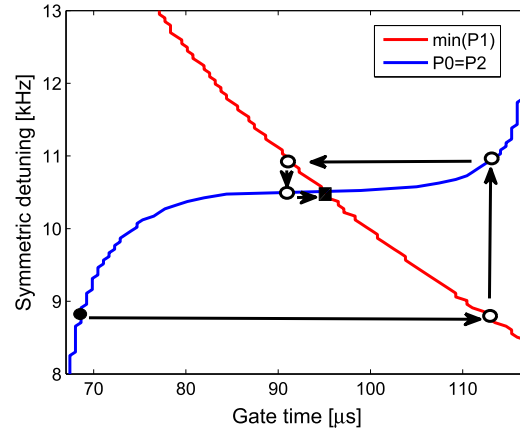


Figure 13. Illustration of the iterative procedure that finds the optimal values for the gate-time and symmetric detuning. The two curves were obtained from the calculated 2D maps of figure 12. The red curve indicates where P_1 is minimal for every value of the symmetric detuning. The blue curve indicates where $P_0 = P_2$ for every value of the gate-time. Starting from a wrong gate-time of $T_{\text{gate}} \approx 70 \mu\text{s}$, we scan the symmetric detuning and set its value where $P_0 = P_1$ (filled black dot). Next, we scan the gate-time with the obtained symmetric detuning and set its new value to where P_1 is minimal (black empty dot). This process is repeated until we converge to the correct values where the two curves cross (black filled rectangle).

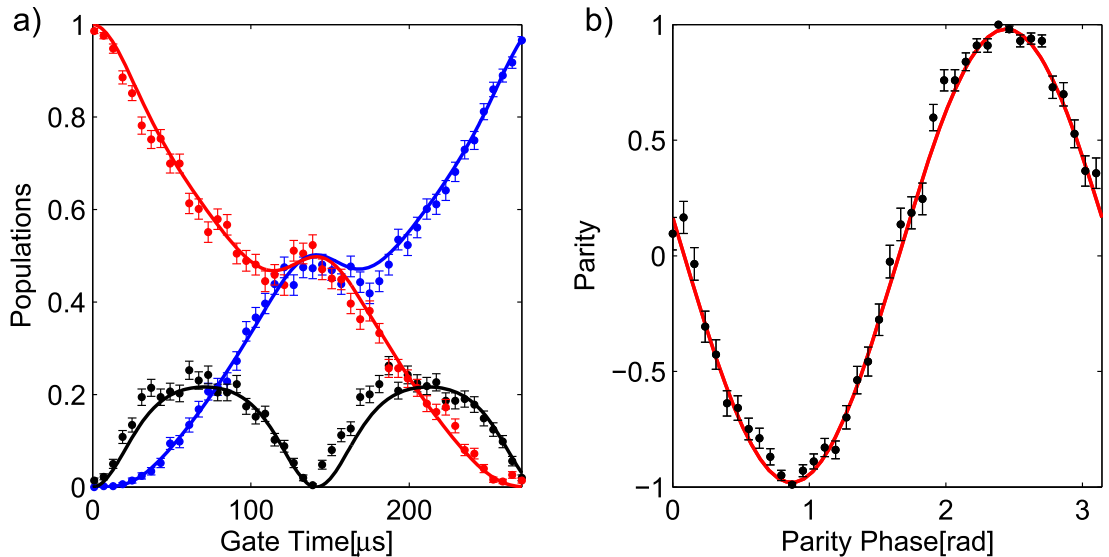


Figure 14. A Mølmer–Sørensen two-qubit gate after optimizing the gate parameters. (a) Populations time evolution as function of the interaction time. (b) Parity oscillation $P = P_0 + P_2 - P_1$ obtained by scanning the phase of a $\pi/2$ pulse at the end of the gate at a gate-time $T_{\text{gate}} = 130 \mu\text{s}$. From these result we infer gate fidelity of $F = 0.985(10)$.

results were consistent with a collective depolarization channel. A possible source of error is off-resonance $|S\rangle \leftrightarrow |D\rangle$ incoherent transition as indicated by the measurement in the inset of figure 4(b).

5. Summary

We presented a universal gate-set for qubits encoded in the electronic states of $^{88}\text{Sr}^+$ ions. The gates were implemented using a narrow linewidth diode laser. Diode lasers have a relatively wide frequency noise spectrum to begin with and therefore are challenging when trying to reach the narrow linewidths required. In particular, we have observed that unlike the case of optical atomic clocks, where noise faster than the linewidth of the laser plays a marginal role, here, residual fast phase noise in the servo-bumps that overlaps the motional sideband transition can generate significant errors to quantum gates. We show that one can overcome this problem by using a high-finesse cavity as a narrow optical filter. This moderates the servo bandwidth requirement and makes an ECDL a compact and affordable solution as a narrow-linewidth laser for QIP. We characterized the laser frequency uncertainty using the ions and found a linewidth below 100 Hz. In order to eliminate the

contribution of the magnetic field noise from the result of a Ramsey experiment we introduced a new type of dynamic modulation sequence. This method may find use in other applications such as atomic clocks that are not based on a magnetic insensitive transition [39, 40]. We demonstrated high-fidelity collective single-qubit gates as well as individual qubit addressing in a two-qubit register by utilizing the inhomogeneous MM-sidebands. Although, this method for individual addressing is limited for only two qubits and not applicable for scalable QIP, we still find it extremely useful in many cases where only two qubits are of interest. For example, we have successfully used this method to measure the magnetic dipole interaction between the spins of two trapped ions [41]. We have implemented a MS two-qubit gate with fidelity of $F = 0.985(10)$, thus realizing a universal gate set for quantum computation with trapped ion qubits.

Acknowledgments

This work was financially supported by the Crown Photonics Center, ICore- Israeli excellence center circle of light, the Israeli Science foundation, the Israeli Ministry of Science Technology and Space, and the European Research Council (consolidator grant 616919-Ionology).

References

- [1] Barenco A, Bennett C H, Cleve R, DiVincenzo D P, Margolus N, Shor P, Sleator T, Smolin J A and Weinfurter H 1995 *Phys. Rev. A* **52** 3457–67
- [2] Zhang J, Vala J, Sastry S and Whaley K B 2003 *Phys. Rev. Lett.* **91** 027903
- [3] Vidal G and Dawson C M 2004 *Phys. Rev. A* **69** 010301
- [4] Home J P, Hanneke D, Jost J D, Amini J M, Leibfried D and Wineland D J 2009 *Science* **325** 1227–30
- [5] Häffner H, Roos C F and Blatt R 2008 *Phys. Rep.* **469** 155–203
- [6] Ospelkaus C, Warring U, Colombe Y, Brown K, Amini J, Leibfried D and Wineland D 2011 *Nature* **476** 181–4
- [7] Langer C *et al* 2005 *Phys. Rev. Lett.* **95** 60502
- [8] Harty T, Allcock D, Ballance C, Guidoni L, Janacek H, Linke N, Stacey D and Lucas D 2014 *Phys. Rev. Lett.* **113** 220501
- [9] Brown K, Wilson A, Colombe Y, Ospelkaus C, Meier A, Knill E, Leibfried D and Wineland D 2011 *Phys. Rev. A* **84** 030303
- [10] Wang S X, Labaziewicz J, Ge Y, Shewmon R and Chuang I L 2009 *Appl. Phys. Lett.* **94** 094103
- [11] Piltz C, Sriarunothai T, Varón A and Wunderlich C 2014 *Nat. Commun.* **5** 4679
- [12] Warring U, Ospelkaus C, Colombe Y, Jördens R, Leibfried D and Wineland D J 2013 *Phys. Rev. Lett.* **110** 173002
- [13] Khromova A, Piltz C, Scharfenberger B, Gloger T F, Johanning M, Varón A F and Wunderlich C 2012 *Phys. Rev. Lett.* **108** 220502
- [14] Benhelm J, Kirchmair G, Roos C and Blatt R 2008 *Nat. Phys.* **4** 463–6
- [15] Ballance C, Harty T, Linke N and Lucas D 2014 arXiv:1406.5473
- [16] Merrill J T *et al* 2011 *New J. Phys.* **13** 103005
- [17] Crain S, Mount E, Baek S and Kim J 2014 *Appl. Phys. Lett.* **105** 181115
- [18] Akerman N, Glickman Y, Kotler S, Keselman A and Ozeri R 2012 *Appl. Phys. B* **107** 1167–74
- [19] Keselman A, Glickman Y, Akerman N, Kotler S and Ozeri R 2011 *New J. Phys.* **13** 073027
- [20] Zhao Y, Zhang J, Stuhler J, Schuricht G, Lison F, Lu Z and Wang L 2010 *Opt. Commun.* **283** 4696–700
- [21] Ludlow A, Huang X, Notcutt M, Zanon-Willette T, Foreman S, Boyd M, Blatt S and Ye J 2007 *Opt. Lett.* **32** 641–3
- [22] Alnis J, Matveev A, Kolachevsky N, Udem T and Hänsch T 2008 *Phys. Rev. A* **77** 053809
- [23] Sterr U, Legero T, Kessler T, Schnatz H, Grosche G, Terra O and Riehle F 2009 Ultrastable lasers: new developments and applications *SPIE Optical Engineering + Applications* (International Society for Optics and Photonics) p 74310A
- [24] Black E D 2001 *Am. J. Phys.* **69** 79–87
- [25] Le Gouët J, Kim J, Bourassin-Bouchet C, Lours M, Landragin A and Pereira Dos Santos F 2009 *Opt. Commun.* **282** 977–80
- [26] Okoshi T, Kikuchi K and Nakayama A 1980 *Electron. Lett.* **16** 630–1
- [27] Roos C, Chwalla M, Kim K, Riebe M and Blatt R 2006 *Nature* **443** 316–9
- [28] Viola L and Lloyd S 1998 *Phys. Rev. A* **58** 2733
- [29] Kotler S, Akerman N, Glickman Y, Keselman A and Ozeri R 2011 *Nature* **473** 61–5
- [30] Kotler S, Akerman N, Glickman Y and Ozeri R 2013 *Phys. Rev. Lett.* **110** 110503
- [31] Riehle F 2004 *Frequency Standards: Basics and Applications* (New York: Wiley)
- [32] Gaebler J P *et al* 2012 *Phys. Rev. Lett.* **108** 260503
- [33] Schindler *et al* 2013 *New J. Phys.* **15** 123012
- [34] Navon N, Kotler S, Akerman N, Glickman Y, Almog I and Ozeri R 2013 *Phys. Rev. Lett.* **111** 073001
- [35] Navon N, Akerman N, Kotler S, Glickman Y and Ozeri R 2014 *Phys. Rev. A* **90** 010103
- [36] Sørensen A and Mølmer K 2000 *Phys. Rev. A* **62** 022311
- [37] Roos C F 2008 *New J. Phys.* **10** 013002
- [38] Kirchmair G, Benhelm J, Zähringer F, Gerritsma R, Roos C and Blatt R 2009 *New J. Phys.* **11** 023002
- [39] Barwood G P, Huang G, Klein H A, Johnson L A M, King S A, Margolis H S, Szymaniec K and Gill P 2014 *Phys. Rev. A* **89** 050501
- [40] Madej A A, Dubé P, Zhou Z, Bernard J E and Gertsvolf M 2012 *Phys. Rev. Lett.* **109** 203002
- [41] Kotler S, Akerman N, Navon N, Glickman Y and Ozeri R 2014 *Nature* **510** 376–80